Microscopic-scale Defect Analysis on β-Ga_2O_3 through Microscopy

Min-Yeong Kim[1,2,3,‡], Andrew J. Winchester[1,‡], Alline F. Myers[4], Edwin J. Heilweil[1], Ory Maimon[1,3], W.-C. David Yang[5], Sang-Mo Koo[2], Qiliang Li[1,3], Sujitra Pookpanratana[1*]

1. Nanoscale Device and Characterization Division, National Institute of Standards and Technology, Gaithersburg, MD 20899
2. Department of Electrical Material Engineering, Kwangwoon University, Seoul 01897, Republic of Korea
3. Department of Electrical Engineering, George Mason University, Fairfax, VA 22030
4. Center for Nanoscale Science and Technology, NIST, Gaithersburg, MD 20899
5. Materials Science and Engineering Division, NIST, Gaithersburg, MD 20899

‡ These authors contributed equally.

*Corresponding author: sujitra@nist.gov

Abstract

β-Ga_2O_3 is a wide bandgap semiconductor with potential for surpassing current-generation high-power device performance and cost-effectiveness, due to its unique properties and availability of large high-quality substrates. However, β-Ga_2O_3 power electronics are still relatively immature, and commercial realization of reliable high-power devices will require intimate knowledge of performance-limiting extended defects. While several defects have been characterized in bulk substrates, less attention has been given to defects in homoepitaxially grown β-Ga_2O_3, despite its importance in producing high quality active layers for power devices. In this work, we characterize the bulk electronic properties and extended structural defects in (010) β-Ga_2O_3 homoepitaxially grown via hydride vapor phase epitaxy (HVPE) using photoemission, transmission electron microscopy (TEM), and complementary spectroscopy and microscopy techniques. We observe two types of linear, surface defects aligned along the [001] crystal axis. One defect consists of a micrometer-sized particle and a tail of protruding material, while the other is a groove in the surface. The large particle is a Ga-rich phase that is likely present early in the HVPE growth that disrupts the surface, while the groove defect appears purely structural in nature. Defect etching and TEM analysis reveal that the linear defects are associated with different dislocation structures, which can explain the different local conductivity measured at each. Our results emphasize that proper surface processing of the bulk substrate is still necessary for obtaining higher quality epitaxial growth for large area power devices.

β-phase gallium oxide (β-Ga_2O_3) is an ultra-wide bandgap material with a bandgap of 4.8 eV [1–4] and a corresponding large breakdown electric field of ~ 8 MV cm^{-1} [5,6] and Baliga's figure of merit of approximately 2870 [7]. Due to the availability of large, high-quality substrates grown from melt, β-Ga_2O_3 has potential cost savings over SiC and GaN technologies in high-power applications [7–9]. β-Ga_2O_3 has begun rapid device development [10–13]; however, several material issues need to be addressed. In SiC, killer defects such as micro pipes, stacking faults, and processing damage were crucial to eliminate for commercial devices [14–16], while threading dislocations[17–19] and stacking faults[20] in GaN have been correlated with device leakage and reliability. Similar issues may also affect β-Ga_2O_3, and several common defects[21] in bulk substrates grown via edge-defined film-fed growth[10,11] and vertical Bridgeman methods[12,13] have been identified and classified. Nanovoid defects have been frequently observed[10,22,23] and are correlated with leakage current, possibly due to forming threading dislocations, in Schottky barrier diodes (SBDs) [23–25]. Other types of dislocations have been observed in β-Ga_2O_3, and some are associated with leakage current in SBDs [10,24], though it is often challenging to identify the exact dislocation type [26].

Only a few reports have examined extended defects in homoepitaxial β-Ga_2O_3 despite its importance in fabricating power devices. Extended defects can be replicated from the substrate into the epitaxial layer, nucleated at the growth interface, or even converted or eliminated under appropriate growth conditions, as in the case for SiC [15,16]. Stacking faults in hydride vapor phase epitaxy (HVPE) growth on (001) surfaces were associated with reverse bias leakage current in SBD devices [27,28]. Dislocations and twin boundaries were observed in plasma-assisted molecular beam epitaxy growth on the $(\bar{2}01)$ surface [29]. Dislocations were also found to form at nanovoids during HVPE growth on (001) surfaces [30]. Linear features and surface roughness due to inadequate polishing and the crystal miscut direction on the (010) surface have also been observed [31]. Defect identification for growth on (010) surfaces has not been investigated in much detail, despite its use as a semi-insulating substrate for lateral RF power devices [8,32].

In this work, we use nanometer-scale, complementary microscopy techniques to identify electrically-active surface defects in n-type (010) β-Ga_2O_3 epitaxy. We find two types of linear defects aligned along the [001] crystal direction: one type is associated with a large particle and surface protrusions (comet), while the other is a groove in the surface (line). The comets are electronically and chemically different from the host β-Ga_2O_3 and lead to reduced local rectification performance. The line defect is not substantially different from β-Ga_2O_3, yet leads to altered local rectification behavior. Wet etching reveals that the defects likely originate early in the epitaxial growth while TEM cross-sectioning reveals different sub-surface dislocation structures.

The β-Ga_2O_3 samples were purchased from Kyma[33] and were comprised of a Si-doped (1×10^{18} cm^{-3}) epilayer (0.4 µm thick) grown by HVPE on a semi-insulating Fe-doped (010) substrate. The typical growth parameters and conditions have been reported[31] , and the dopant source is likely SiH_4 in 0.2% N_2 and the β-Ga_2O_3 precursors of HCl or Cl_2/H_2 with liquid gallium and O_2 (19.5% O_2 in N_2) are likely used. Ultraviolet (UPS) and x-ray (XPS) photoemission spectroscopy were taken using He I and monochromatic Al k_α excitations, respectively. The photoemission electron microscope (PEEM) has been described in detail elsewhere[34,35] and used an excitation wavelength of 193 nm (6.4 eV) or 210 nm (5.9 eV). Topography and current images were measured using (conductive) atomic force microscopy (AFM or cAFM) with a heavily-doped diamond coated probe (100 nm tip radius). Scanning electron microscopy (SEM) energy dispersive x-ray spectroscopy (EDS) was used for elemental analysis at electron beam energies of 2 kV, 5 kV, and 10 kV. Defect etching was performed in 14 mol L^{-1} H_3PO_4 at 400 K (125 °C). A home-built terahertz time-domain spectroscopy (THz-TDS) setup was used to measure the average epi-layer conductivity[36]. Cross-sectional lamella were prepared using Ga ion beam milling in a FEI Helios 660 Dual Beam FIB-SEM [33].

TEM imaging was performed at 300 kV in a FEI Titan 80-300 S/TEM [33]. Further details about sample preparation and measurements are in the Supplemental Information.

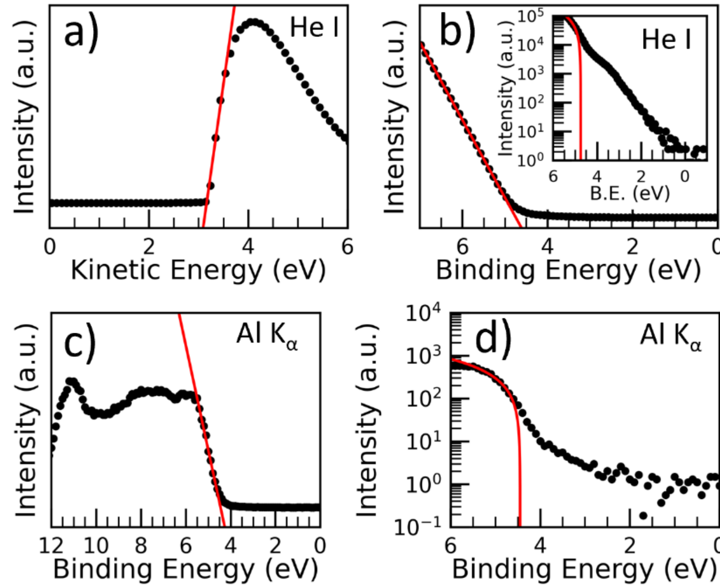

Figure 1. PES measurements of a) the secondary electron cutoff and the valence band edge of the epitaxial β-Ga_2O_3 using b) He I, c) and d) Al K_α excitations. The valence band in b) and c) are in linear scale, while d) and inset of b) are on semi-log scales. The red lines are linear fits of the data.

We first assess the macroscopic surface electronic properties of the homoepitaxy (010) film. From the secondary electron cutoff of the photoemission spectrum (PES) (Figure 1a), a work function (φ) of 3.16 eV ± 0.05 eV is determined. The valence band maximum (VBM) extracted from Figure 1b is at 4.75 eV ± 0.05 eV below the Fermi energy, and indicates that the film should be nearly degenerately doped, as expected. The VBM estimated from XPS (Figure 1c) is shallower at 4.5 eV ± 0.1 eV, which may be due to cross section differences between XPS and UPS and the flat valence band dispersion [37]. The calculated ionization potential and electron affinity (EA) from UPS (assuming a 4.8 eV band gap) are 7.91 eV ± 0.07 eV and 3.11 eV ± 0.07 eV, respectively. φ and EA are similar to a recent work[38] and in reasonable agreement with calculations [39]. The VBM with both He I (Figure 1b inset) and Al K_α excitation (Figure 1d) also indicate tail states extending into the band gap, which have previously been observed in epi-ready, cleaved, and epitaxially grown β-Ga_2O_3 [38,40,41] and are likely due to point defects and impurities. This macroscopic electronic structure of a heavily doped surface is consistent with the average conductivity of 23 S cm^{-1} (or 0.044 Ω cm layer resistance) estimated using THz-TDS between 0.7 THz and 1.3 THz (Supplementary Figure S1) which is comparable to another report[42].

PEEM is used to assess the local electronic properties of the epitaxy surface, and shows parallel lines several tens of micrometers in length on the sample (Figure 2a) that occasionally occur in clusters or bands (Supplementary Figure S2). We observe two different linear features: one with a micrometer size particle at one end (orange circles in Figure 2a, "comet"), and another without any particle (blue circle in Figure 2a, "line"). Higher magnification PEEM images of comet and line defects are shown in Figures 2b and 2c, respectively, and they occur with densities of approximately 10^3 cm^{-2} and $<10^5$ cm^{-2}, respectively. A piece

of the substrate without any epitaxial growth did not contain any of these defects (Supplementary Figure S3); therefore, the comet and line defects likely develop during the HVPE epitaxial growth.

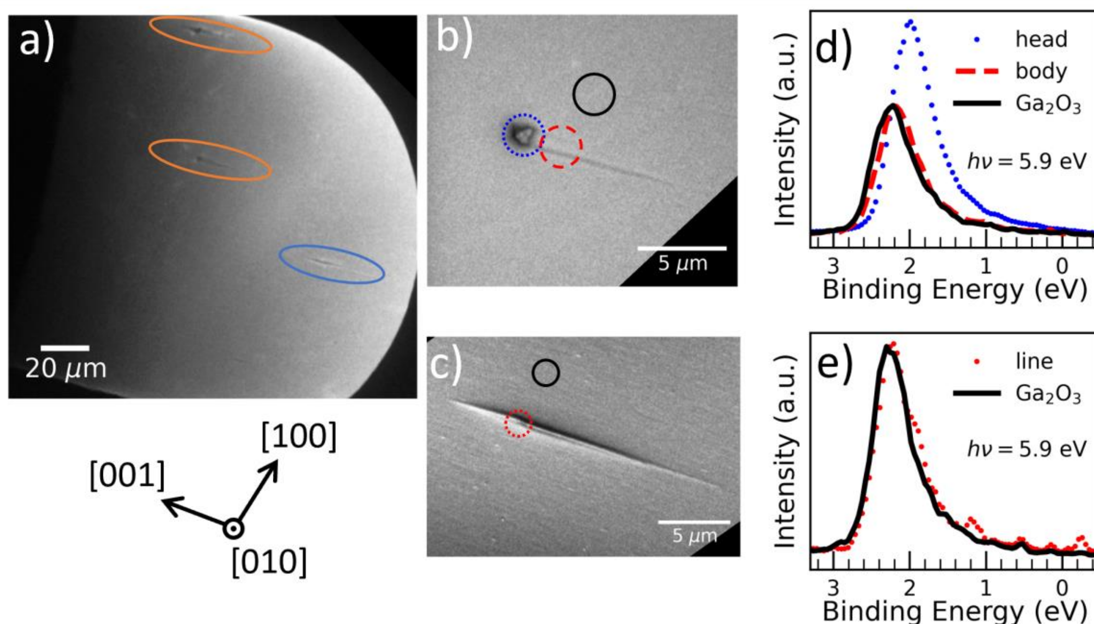

Figure 2. PEEM observations of a) comet and line defects circled in orange and blue, respectively, and at higher magnification at b) a comet and c) a line defect. PEEM PES spectrum from the areas marked by solid and dashed circles in b) and c) for d) a comet defect and e) a line defect, respectively. For d) and e), the work function measured with He I UPS was used to convert to an approximate binding energy scale (see Supplementary Information).

Each defect is examined separately in more detail using micro-spectroscopy in the PEEM. The low photon energy of ~ 6 eV used (notably below the ionization potential determined with UPS) indicates that PEEM probes occupied gap states and not the valence band directly. We observe a shift and broadening of the photoemission spectrum at lower binding energies on the comet head and a slight shift on the body, relative to the surrounding β-Ga_2O_3 (Figure 2d). This indicates additional gap states and a larger work function at the head, suggesting that it is a different composition. In contrast, the line defect does not show any significant difference of the surface electronic structure compared to the surrounding β-Ga_2O_3 (Figure 2e).

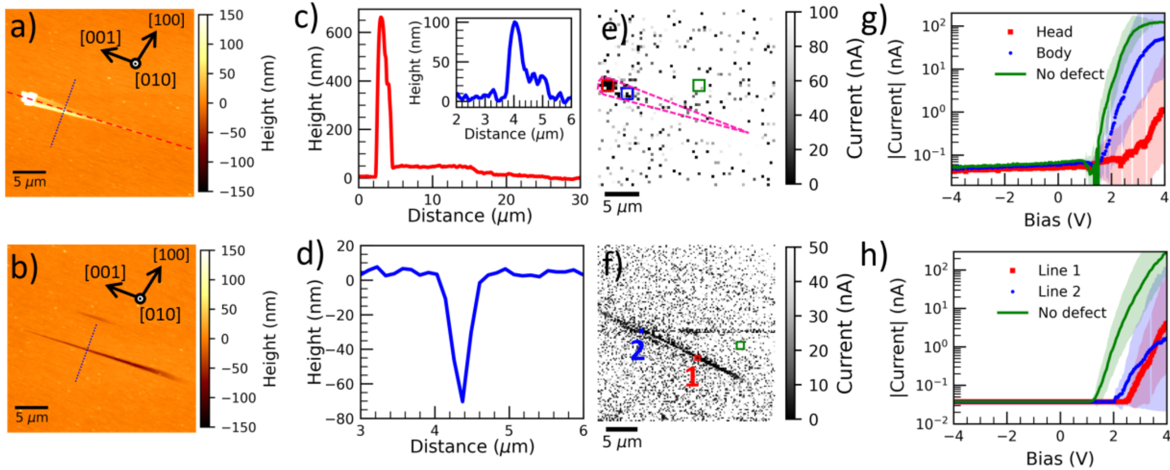

Figure 3. AFM topography of a) the comet defect and b) the line defect. Height profiles of c) the comet defect and d) the line defect along the dashed lines from a) and b), respectively. cAFM current images at +3.5 V bias for e) the comet and f) the line defect. The comet defect position is outlined by the magenta dashed line as a guide. Current-voltage plots in g) and h) are from red, blue, and green boxes in e) and f), respectively. Red and blue boxes are regions on the defect, while the green box is a 'no defect' region. The shaded areas of the I-V curves represent the geometric standard deviation factors.

The same areas observed in PEEM were characterized by AFM and cAFM. Figure 3a shows the topography of the comet defect, where the head of the comet defect and the tail of the defect have a raised height relative to the substrate. In contrast, the line defect corresponds to a groove in the surface, as shown in Figure 3b. The topography profiles of the comet and line defects in Figure 3c and 3d, respectively, indicate that the body of the comet is approximately 100 nm taller than the surrounding material, while the line defect is approximately 75 nm deep. The head of the comet is taller at approximately 600 nm. Consequently, the image contrast of these defects in PEEM is primarily due to topographic effects, where the disturbance of the acceleration field deflects the photoelectrons and modulates contrast [43,44].

Through cAFM, we investigated the defects' electrical conductivities. For the comet and line defects shown in Figures 3a and 3b, we find that the forward current at +3.5 V bias is significantly reduced at the head of the comet defect and the line defect, as shown in Figures 3e and 3f, respectively (see Supplementary Figure S4 for other bias voltages). For the comet defect, I-V curves extracted from the head and body and compared against the surrounding β-Ga_2O_3 (red, blue, and green boxes in Figure 3e, respectively) are shown in Figure 3g and display rectifying Schottky behavior, as expected. The forward turn on voltage is increased and the current is reduced by almost three and one order of magnitude at the head and the body of the defect, respectively, compared to the bare β-Ga_2O_3 region. I-V curves from multiple positions of the line defect, as

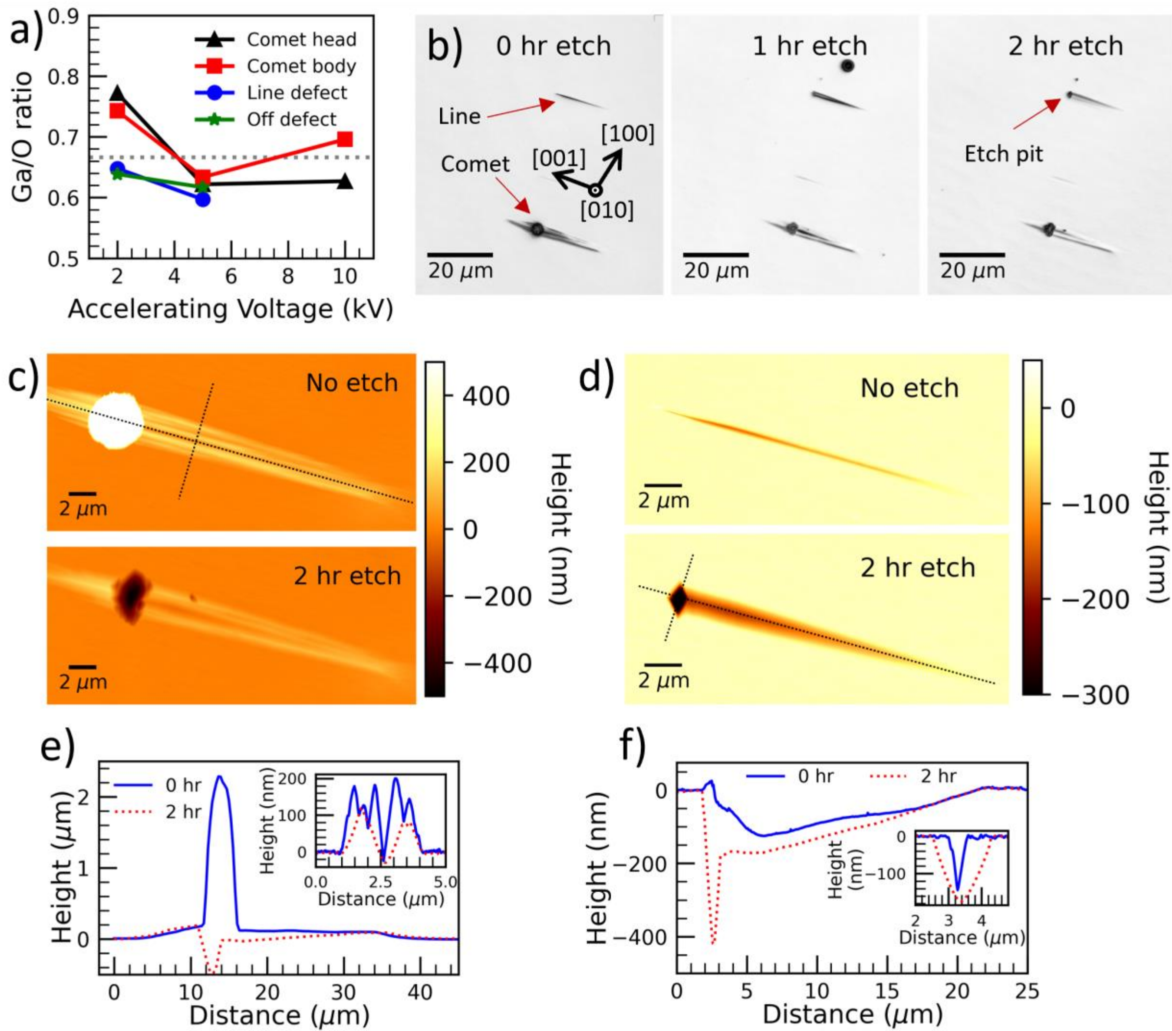

Figure 4. EDS and etch analysis. a) SEM EDS measurements of the Ga/O ratio at different accelerating voltages on and off of the comet and line defects. The dotted grey line in a) represents the ideal Ga/O ratio of 2/3. b) Sequential confocal microscopy images of a comet and line defect before and after etching in H_3PO_4 at 400 K (125 °C). AFM topography before and after etching of c) a comet defect and d) a line defect. AFM height profiles measured along the dotted lines in (c) and (d) before and after etching for the long and short axes (insets) of e) the comet defect and f) the line defect.

shown in Figure 3h, show an increased turn on voltage and a reduction in the forward current by approximately two orders of magnitude compared to the surrounding β-Ga_2O_3.

Using SEM-EDS, we find that the head and body of the comet are gallium rich and oxygen poor relative to the surrounding β-Ga_2O_3 (Figure 4a) at the surface (2 kV acceleration voltage) and no other metals were detected in the particle. Along with the energy changes measured in PEEM, this indicates that the head is of non-stoichiometric composition. In contrast, the line defect shows no substantial difference in the Ga to O ratio, which agrees with the PEEM spectroscopy results that the line defect is mainly a structural defect.

The structural characteristics and origins of the defects were assessed by etching the thin-film in phosphoric acid. Sequential etching for 1 hr and 2 hr causes changes in both comet and line defects, as shown in the confocal microscope images in Figure 4b[10,22]. The particle at the head is completely etched away on the comet defect (Figure 4c), leaving a pit with a depth comparable to the epilayer thickness (Figure 4e), while the body only slightly changes. Therefore, this particle was likely either on the substrate before or formed at the beginning of the epitaxial growth. In contrast, the line defect (Figures 4d and 4f) widens and deepens after etching, particularly at the end that forms a polygonal pit. The pit is comparable in depth to the epilayer thickness (Figure 4f) and it converges to a point, likely indicating a threading dislocation (TD) [22,26]. However, only approximately 75% of the line defects formed polygonal etch pits.

Bright-field TEM images (Figures 5 a and e) confirm the tomographic profiles and that the comet and line defects are aligned along the [001] direction, in agreement with the substrate cleaving direction and literature on the HVPE growth [31]. Both defects show regions of dark contrast below them suggesting local disorder due to dislocations, which was analyzed using weak-beam dark field (WBDF) TEM. Imaging the comet defect at **g** = (310) reveals bright, short horizontal dislocation lines (less than 40 nm in length) that are aligned to form parallel stripes through the entire thickness of the epilayer, as indicated with the green arrows in Figure 5b. However, for **g** = $(82\bar{1})$ the dislocation contrast disappears (Figure 5c). The contrast invisibility suggests that the horizontal dislocation lines are the pure edge components of prismatic dislocation loops (PDL) with a Burgers vector **b** = <010>. Some of the stripes terminate with vertical dislocation lines near the top surface of the epilayer (indicated by cyan arrows in Figure 5c) which are screw-type TDs with **b** = <010>. Figure 5d illustrates the alignment of individual PDLs into a stripe, which occurs when a screw-type TD climbs during the epitaxial growth [45]. The screw-type TDs and stripes formed by the PDLs start from the substrate interface (as indicated with the green dashed lines in Figure 5a) and are not present in the substrate. This comet defect has not been reported before for β-Ga_2O_3; however, it resembles comet defects and polytype inclusions ("downfall particles") in SiC, which are known to be killer defects in devices [14,15,46–48]. Therefore, this defect is likely due to a non-stoichiometric gallium oxide particle disrupting the epitaxial growth, which results in the formation and climb of nearby dislocations due to the associated strain[49]. Similar issues due to particles causing extended defects have previously been observed for (001) β-Ga_2O_3 epitaxy [27,50].

The line defect displays similar short horizontal lines made of the edge-type components of dislocation loops but without the same vertical alignment when imaged using a weak beam at **g** = (020), as indicated

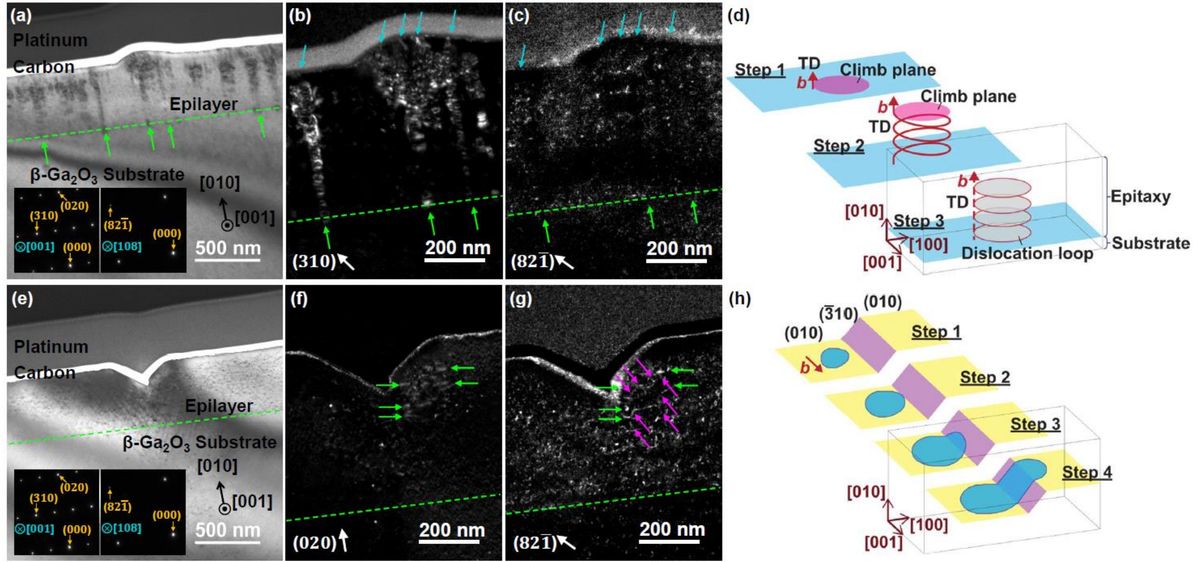

Figure 5. Dislocation analysis using weak-beam dark-field (WBDF) TEM imaging for comet (a-d) and line (e-h) defects. Cross-sectional bright-field TEM images of a (a) comet and (e) line defect obtained near the [001] zone axis at the two-beam condition with the (310) reflection. The insets show the electron diffraction patterns at the [001] and [108] zone axes. WBDF TEM images of the (b) comet and (f) line defects acquired using at the reflections g = (310) and g = (020), respectively, near the [001] zone axis showing the phase contrast of dislocation loops. WBDF TEM images of the (c) comet and (g) line defects at the reflection g = (82$\bar{1}$) near the [108] zone axis showing the elimination (c) or addition (g) of phase contrast based on the invisibility criteria. The dashed lines in (a-c) and (e-g) indicate the epitaxy – substrate interface. Schematics of (d) threading dislocation (TD) climb resulting in the alignment of dislocation loops near the comet defect, and (h) of dislocation loop cross-slip leading to the formation of dislocation jogs near the line defect.

with the green arrows in Figure 5f. Additional short vertical lines appear (indicated by the magenta arrows in Figure 5g) that connect with the dislocation loops when imaged at **g** = (82$\bar{1}$). The invisibility of the vertical lines with **g** = (020) suggests that the dislocation loops have a **b** with mixed direction components involving <001>. The screw-type part of a dislocation loop, where **u** is parallel to **b**, can glide on a primary {010} plane and cross-slip to a secondary {$\bar{3}$10} plane [51], followed by a double cross-slip back to another primary slip plane to form the dislocation jog, as sketched in Figure 5h. This results in a complex dislocation network near the line defect as seen in Figure 5f, which is the likely cause of reduced conductivity, as dislocations are known recombination centers in GaN [17,18], SiC [16], and possibly β-Ga_2O_3 [52]. Voids, grooves, and lines on β-Ga_2O_3 due to nanovoid defects in bulk crystals are associated with increased leakage current [10,22,23]. However, the etch pits observed at line defects (Figure 4d) do not match those of nanovoids, which were observed separately (Supplementary Figure S5). Subsurface processing damage may be a cause of this defect since it does not clearly nucleate at the epitaxy-substrate interface [25,31,53–55]. We surmise that the line defect could be eliminated by chemical mechanical polishing (CMP), as it extends about 75 nm below the surface and CMP has been effective of removing material[54,56]. However, the CMP process would need to be optimized to care for the brittleness of β-Ga2O3, and inadequate polishing leads to a higher density of surface defects[55], substantial sub-surface damage that affects device leakage[25], and causes issues with epitaxial growth[31]. Given the moderate density, lateral size, and electrical properties of the line defects, they

are likely responsible for anomalous and spatially varying device behavior, such as that observed in β-Ga_2O_3 MOSFET devices [57].

We have observed and characterized two types of linear defects aligned along the [001] direction on HVPE grown homoepitaxial (010) β-Ga_2O_3. The comet defect consists of a particle and protruding material from the surface that occurs with a density of 10^3 cm^{-2} and causes a lower conductivity. In contrast, the line defect is a groove in the surface without any significant chemical or electronic changes at the surface that occurs with a density of 10^5 cm^{-2}. The comet and line defects are associated with dislocation loops undergoing climb and cross-slip, respectively, in the epitaxial film. The dense network of dislocations below the line defect likely explains the substantially lower current measured locally for a Schottky contact with the AFM tip. Our results suggest that the comet defects are formed early in the HVPE growth; therefore, better control of surface processing and the initial growth environment are essential for obtaining higher quality epitaxy.

See the supplemental material for details on sample preparation, measurement details and supporting results.

A.J.W. was supported by the NRC Postdoctoral Associateship program. M.K. was supported by the Korean Power Electronics Consortium with KETEP grant. O.M. is supported through the GMU Presidential Scholarship Award. M.K. and O.M. acknowledge partial support from the NIST MSE grant 70NANB23H093. The research was performed in part at the NIST Center for Nanoscale Science and Technology, and we thank Kerry Siebein and Joshua Schumacher for SEM-EDX and FIB support, respectively.

Author declarations section

The authors have no conflicts to disclose.

Author Contributions

M.-Y. Kim: Conceptualization (equal), Data curation (equal), Formal analysis (equal), Investigation (equal), Methodology (equal), Writing – Original draft preparation (supporting), Writing – review & editing (equal); **A. Winchester**: Conceptualization (equal), Data curation (equal), Formal analysis (equal), Investigation (equal), Methodology (equal), Visualization (equal), Writing – original draft preparation (equal), Writing – review & editing (equal); **A. F. Myers**: Data curation (equal), Formal analysis (equal), Investigation (supporting), Methodology (equal), Writing – review & editing (equal); **E. J. Heilweil**: Data curation (equal), Formal analysis (equal), Investigation (supporting), Methodology (equal), Writing – review & editing (equal); **O. Maimon**: Investigation (supporting), Writing – review & editing (equal); **W.-C. David Yang**: Data curation (equal), Formal analysis (equal), Investigation (supporting), Methodology (equal), Writing – original draft preparation (supporting), Writing – review & editing (equal); **S.-M. Koo**: Funding acquisition (equal), Project administration (equal), Supervision (equal), Writing – review & editing (equal); **Q. Li**: Funding acquisition (equal), Project administration (equal), Supervision (equal), Writing – review & editing (equal); **S. Pookpanratana**: Conceptualization (equal), Data curation (equal), Formal analysis (equal), Funding acquisition (equal), Investigation

(supporting), Methodology (equal), Project administration (equal), Supervision (equal), Visualization (equal), Writing - original draft preparation (equal), Writing – review & editing (equal).

Data availability

The data to support the findings of this study are available from the corresponding author upon reasonable request.

References

1. Tippins, H. H. Optical Absorption and Photoconductivity in the Band Edge of β−Ga2O3. *Physical Review* **140**, A316–A319 (1965).
2. Ueda, N., Hosono, H., Waseda, R. & Kawazoe, H. Anisotropy of electrical and optical properties in β-Ga2O3 single crystals. *Appl Phys Lett* **71**, 933–935 (1997).
3. He, H. *et al.* First-principles study of the structural, electronic, and optical properties of Ga2O3 in its monoclinic and hexagonal phases. *Phys Rev B* **74**, 195123 (2006).
4. Onuma, T. *et al.* Valence band ordering in β-Ga 2 O 3 studied by polarized transmittance and reflectance spectroscopy. *Jpn J Appl Phys* **54**, 112601 (2015).
5. Higashiwaki, M., Sasaki, K., Kuramata, A., Masui, T. & Yamakoshi, S. Gallium oxide (Ga2O3) metal-semiconductor field-effect transistors on single-crystal β-Ga2O3 (010) substrates. *Appl Phys Lett* **100**, 1–4 (2012).
6. Higashiwaki, M. & Jessen, G. H. Guest Editorial: The dawn of gallium oxide microelectronics. *Appl Phys Lett* **112**, (2018).
7. Pearton, S. J., Ren, F., Tadjer, M. & Kim, J. Perspective: Ga 2 O 3 for ultra-high power rectifiers and MOSFETS. *J Appl Phys* **124**, 220901 (2018).
8. Maimon, O. & Li, Q. Progress in Gallium Oxide Field-Effect Transistors for High-Power and RF Applications. *Materials* **16**, 7693 (2023).
9. Heinselman, K. N., Haven, D., Zakutayev, A. & Reese, S. B. Projected Cost of Gallium Oxide Wafers from Edge-Defined Film-Fed Crystal Growth. *Cryst Growth Des* **22**, 4854–4863 (2022).
10. Ueda, O. *et al.* Structural evaluation of defects in β-Ga 2 O 3 single crystals grown by edge-defined film-fed growth process. *Jpn J Appl Phys* **55**, 1202BD (2016).
11. Ueda, O., Kasu, M. & Yamaguchi, H. Structural characterization of defects in EFG- and HVPE-grown β-Ga 2 O 3 crystals. *Jpn J Appl Phys* **61**, 050101 (2022).
12. Ohba, E., Kobayashi, T., Kado, M. & Hoshikawa, K. Defect characterization of β-Ga 2 O 3 single crystals grown by vertical Bridgman method. *Jpn J Appl Phys* **55**, 1202BF (2016).
13. Ohba, E., Kobayashi, T., Taishi, T. & Hoshikawa, K. Growth of (1 0 0), (0 1 0) and (0 0 1) β-Ga2O3 single crystals by vertical Bridgman method. *J Cryst Growth* **556**, 125990 (2021).
14. Das, H., Sunkari, S. & Naas, H. Classification of Killer and Non-Killer Silicon Carbide Epitaxial Defects and Accurate Prediction of Device Yield. *ECS Meeting Abstracts* **MA2017-02**, 1345–1345 (2017).
15. Chen, P.-C. *et al.* Defect Inspection Techniques in SiC. *Nanoscale Res Lett* **17**, 30 (2022).
16. Li, J. *et al.* Dislocations in 4H silicon carbide. *J Phys D Appl Phys* **55**, 463001 (2022).

17. Cameron, D. *et al.* The influence of threading dislocations propagating through an AlGaN UVC LED. *Appl Phys Lett* **120**, 162101 (2022).

18. Besendörfer, S. *et al.* The impact of dislocations on AlGaN/GaN Schottky diodes and on gate failure of high electron mobility transistors. *Sci Rep* **10**, 17252 (2020).

19. Usami, S. *et al.* Correlation between nanopipes formed from screw dislocations during homoepitaxial growth by metal-organic vapor-phase epitaxy and reverse leakage current in vertical p–n diodes on a free-standing GaN substrates. *Jpn J Appl Phys* **58**, SCCB24 (2019).

20. Song, J. *et al.* Elimination of Stacking Faults in Semipolar GaN and Light-Emitting Diodes Grown on Sapphire. *ACS Appl Mater Interfaces* **11**, 33140–33146 (2019).

21. Fu, B. *et al.* A review of β -Ga 2 O 3 single crystal defects, their effects on device performance and their formation mechanism. *Journal of Semiconductors* **40**, 011804 (2019).

22. Hanada, K. *et al.* Origins of etch pits in β-Ga 2 O 3 (010) single crystals. *Jpn J Appl Phys* **55**, 1202BG (2016).

23. Sdoeung, S. *et al.* Origin of reverse leakage current path in edge-defined film-fed growth (001) β -Ga2O3 Schottky barrier diodes observed by high-sensitive emission microscopy. *Appl Phys Lett* **117**, 3–7 (2020).

24. Kasu, M. *et al.* Relationship between crystal defects and leakage current in β-Ga 2 O 3 Schottky barrier diodes. *Jpn J Appl Phys* **55**, 1202BB (2016).

25. Sdoeung, S. *et al.* Line-shaped defects: Origin of leakage current in halide vapor-phase epitaxial (001) β -Ga2O3 Schottky barrier diodes. *Appl Phys Lett* **120**, 1–5 (2022).

26. Yao, Y., Sugawara, Y. & Ishikawa, Y. Observation of dislocations in β -Ga 2 O 3 single-crystal substrates by synchrotron X-ray topography, chemical etching, and transmission electron microscopy. *Jpn J Appl Phys* **59**, 045502 (2020).

27. Sdoeung, S. *et al.* Stacking faults: Origin of leakage current in halide vapor phase epitaxial (001) β -Ga 2 O 3 Schottky barrier diodes. *Appl Phys Lett* **118**, 172106 (2021).

28. Ogawa, K., Kobayashi, K., Hasuike, N. & Isshiki, T. Crystal structure analysis of stacking faults through scanning transmission electron microscopy of β-Ga2O3 (001) layer grown via halide vapor phase epitaxy. *Journal of Vacuum Science & Technology A* **40**, (2022).

29. Ngo, T. S. *et al.* Investigation of defect structure in homoepitaxial (-201) b-Ga2O3 layers prepared by plasma-assisted molecular beam epitaxy. *J Alloys Compd* **834**, 155027 (2020).

30. Masuya, S. *et al.* Characterization of crystalline defects in β -Ga 2 O 3 single crystals grown by edge-defined film-fed growth and halide vapor-phase epitaxy using synchrotron X-ray topography. *Jpn J Appl Phys* **58**, 055501 (2019).

31. Leach, J. H. *et al.* Halide vapor phase epitaxial growth of β-Ga2O3 and α-Ga2O3 films. *APL Mater* **7**, (2019).

32. Blevins, J. D., Stevens, K., Lindsey, A., Foundos, G. & Sande, L. Development of Large Diameter Semi-Insulating Gallium Oxide (Ga 2 O 3) Substrates. *IEEE Transactions on Semiconductor Manufacturing* **32**, 466–472 (2019).

33. The identification of commercial equipment or vendor is not intended to imply recommendation or endorsement by NIST, nor is it intended to imply that the materials or equipment identified are necessarily the best available for the purpose.

34. Niefind, F. *et al.* Imaging and measuring the electronic properties of epitaxial graphene with a photoemission electron microscope. *J Appl Phys* **131**, 015303 (2022).

35. Winchester, A. J., Anderson, T. J., Hite, J. K., Elmquist, R. E. & Pookpanratana, S. Methodology and implementation of a tunable deep-ultraviolet laser source for photoemission electron microscopy. *Ultramicroscopy* **253**, 113819 (2023).

36. Magnanelli, T. J. *et al.* Polarization Dependence of Charge Conduction in Conjugated Polymer Films Investigated with Time-Resolved Terahertz Spectroscopy. *The Journal of Physical Chemistry C* **124**, 6993–7006 (2020).

37. Swallow, J. E. N. *et al.* Transition from electron accumulation to depletion at β-Ga2O3 surfaces: The role of hydrogen and the charge neutrality level. *APL Mater* **7**, (2019).

38. Chikoidze, E. *et al.* Surface two-dimensional hole gas in Si doped β-Ga2O3 thin film. *J Alloys Compd* **971**, 172713 (2024).

39. Mu, S., Peelaers, H., Zhang, Y., Wang, M. & Van de Walle, C. G. Orientation-dependent band offsets between (Al x Ga1− x)2O3 and Ga2O3. *Appl Phys Lett* **117**, (2020).

40. Michling, M. & Schmeißer, D. Resonant Photoemission at the O1s threshold to characterize β-Ga 2 O 3 single crystals. *IOP Conf Ser Mater Sci Eng* **34**, 012002 (2012).

41. Navarro-Quezada, A. *et al.* Surface properties of annealed semiconducting β-Ga2O3 (1 0 0) single crystals for epitaxy. *Appl Surf Sci* **349**, 368–373 (2015).

42. Blumenschein, N. *et al.* Dielectric and conducting properties of unintentionally and Sn-doped β -Ga2O3 studied by terahertz spectroscopy. *J Appl Phys* **127**, (2020).

43. Lavayssière, M., Escher, M., Renault, O., Mariolle, D. & Barrett, N. Electrical and physical topography in energy-filtered photoelectron emission microscopy of two-dimensional silicon pn junctions. *J Electron Spectros Relat Phenomena* **186**, 30–38 (2013).

44. Stohr, J. & Anders, S. X-ray spectro-microscopy of complex materials and surfaces. *IBM J Res Dev* **44**, 535–551 (2000).

45. Strunk, H., Gösele, U. & Kolbesen, B. O. Interstitial Supersaturation And Climb Of Misfit Dislocations In Phosphorus-Diffused Silicon. *J Microsc* **118**, 35–39 (1980).

46. Long, H. *et al.* Understanding the breakdown asymmetry of 4H-SiC power diodes with extended defects at locations along step-flow direction. *J Appl Phys* **128**, (2020).

47. Lee, K.-Y. & Capano, M. A. The Correlation of Surface Defects and Reverse Breakdown of 4H-SiC Schottky Barrier Diodes. *J Electron Mater* **36**, 272–276 (2007).

48. Yamashita, T. *et al.* Characterization of comet-shaped defects on C-face 4H-SiC epitaxial wafers by electron microscopy. *J Cryst Growth* **416**, 142–147 (2015).

49. Hull, D. & Bacon, D. J. Origin and Multiplication of Dislocations. *Introduction to Dislocations* 157–169 (2011) doi:10.1016/b978-0-08-096672-4.00008-6.

50. Sdoeung, S. *et al.* Polycrystalline defects—origin of leakage current—in halide vapor phase epitaxial (001) β-Ga 2 O 3 Schottky barrier diodes identified via ultrahigh sensitive emission microscopy and synchrotron X-ray topography. *Applied Physics Express* **14**, 036502 (2021).

51. Yamaguchi, H., Kuramata, A. & Masui, T. Slip system analysis and X-ray topographic study on β-Ga2O3. *Superlattices Microstruct* **99**, 99–103 (2016).

52. Haven, D. *et al.* Multimodal microscopy of extended defects in β-Ga2O3 (010) EFG crystals. *AIP Adv* **13**, 1–5 (2023).

53. Sdoeung, S. *et al.* Observation of comet-shaped defect as killer defect in halide vapor phase epitaxial (001) β-Ga 2 O 3 and its impact on Schottky barrier diodes. *Jpn J Appl Phys* **62**, 071001 (2023).

54. Liao, M. E., Huynh, K., Matto, L., Luccioni, D. P. & Goorsky, M. S. Optimization of chemical mechanical polishing of (010) β-Ga2O3. *Journal of Vacuum Science & Technology A* **41**, (2023).

55. Perrier, C. *et al.* Surface defects related to polishing cycle in ß-Ga2O3 crystals grown by floating zone. *Appl Phys Lett* **122**, 1–6 (2023).

56. Lavelle, R. M. *et al.* Chemical-mechanical polishing improvements and subsurface damage elimination for Cz grown (010) β-Ga2O3 substrates. *Mater Sci Semicond Process* **190**, 109341 (2025).

57. Maimon, O. *et al.* Measurement and gate-voltage dependence of channel and series resistances in lateral depletion-mode β-Ga 2 O 3 MOSFETs. *Semicond Sci Technol* **38**, 075016 (2023).